Published in final edited form as:
J Med Robot Res. 2022 ; 7(2-3): . doi:10.1142/s2424905x22410057.

Design of a 6-DoF Parallel Robotic Platform for MRI Applications

Mishek Musa, B.S., M.S[*], **Saikat Sengupta, B.S., M.Sc., Ph.D.**[†], **Yue Chen, B.S., M.Phil., Ph.D.**[‡,§]

[*]Department of Mechanical Engineering, University of Arkansas, Fayetteville, AR 72701, USA

[†]Vanderbilt University Institute of Imaging Science, Vanderbilt University Medical Center, Nashville, TN 37232, USA

[‡]Department of Biomedical Engineering, Georgia Institute of Technology/Emory University, Atlanta, GA 30332, USA

Abstract

In this work, the design, analysis, and characterization of a parallel robotic motion generation platform with 6-degrees of freedom (DoF) for magnetic resonance imaging (MRI) applications are presented. The motivation for the development of this robot is the need for a robotic platform able to produce accurate 6-DoF motion inside the MRI bore to serve as the ground truth for motion modeling; other applications include manipulation of interventional tools such as biopsy and ablation needles and ultrasound probes for therapy and neuromodulation under MRI guidance. The robot is comprised of six pneumatic cylinder actuators controlled via a robust sliding mode controller. Tracking experiments of the pneumatic actuator indicates that the system is able to achieve an average error of 0.69 ± 0.14 mm and 0.67 ± 0.40 mm for step signal tracking and sinusoidal signal tracking, respectively. To demonstrate the feasibility and potential of using the proposed robot for minimally invasive procedures, a phantom experiment was performed in the benchtop environment, which showed a mean positional error of 1.20 ± 0.43 mm and a mean orientational error of 1.09 ± 0.57°, respectively. Experiments conducted in a 3T whole body human MRI scanner indicate that the robot is MRI compatible and capable of achieving positional error of 1.68 ± 0.31 mm and orientational error of 1.51 ± 0.32° inside the scanner, respectively. This study demonstrates the potential of this device to enable accurate 6-DoF motions in the MRI environment.

Keywords

MRI; parallel robot; motion generation

1. Introduction

Magnetic Resonance Imaging (MRI) is a leading diagnostic and research imaging tool that presents several key benefits over other imaging modalities. The primary advantage is that MRI diminishes exposure of patients or clinicians to ionizing radiation. Additionally, MRI

[§] yue.chen@bme.gatech.edu .

allows for excellent soft tissue contrasts and unique multiplanar imaging capabilities [1]. These benefits make MRI an excellent choice for deep tissue imaging and image-guided interventions. For both routine diagnostic imaging, as well as for interventional applications, there exists a need for robotic motion platforms capable of producing complex automated motions inside the MRI scanner. In the first case, this is motivated by the need to accurately create a generalized motion device and use it as the benchmark to validate the motion correction algorithms [2, 3]. In the second, this is motivated by the need to remotely and accurately drive interventional devices such as biopsy needles, ablation probes or brachytherapy stylets at a desired pose towards an arbitrary target within the body [4–6]. Both have remained a challenge for the conventional robots fabricated with DC motors due to the difficult electromagnetic (EM) environment and space restrictions of standard MRI scanners.

Some efforts have been made in the past to develop devices to impart accurate motions within the MRI scanner. Steinmann et al. demonstrated a dynamic MRI/computed tomography (CT) compatible anthropomorphic thorax phantom for use in MR image-guided radio-therapy. A 1-degree of freedom (DoF) motion platform was developed by Nofiele *et al*. for motion management studies in MRI [7]. Additionally, several commercial phantom devices have been developed for motion management studies in the MRI environment [8–10]. These systems, however, either lack sufficient DoF or are not general enough to be applied to different motion applications.

MRI compatible robotics is a field that has made great strides in accurate motion generation in the MR environment. Many robots have been designed to perform a wide variety of MR-guided interventional inside MRI scanner. These interventions include prostate ablation [5], gynecologic brachytherapy [11], epilepsy ablation [12], intracerebral hemorrhage removal [13], breast biopsy and intervention [14], and many others [15]. The predominant challenge facing MRI-compatible robotics is that as a result of the high magnetic field strengths, ferromagnetic materials used to develop traditional robots cannot be included [1]. It is essential for a robot to meet the MR conditionality criteria outlined by the American Society for Testing and Materials (ASTM) so that it may be deployed in the MR environment [16]. Many MR-compatible robots, for example, have been constructed using piezoelectric motors. These include a parallel robot that was created to enable 4-DoF control of an intraspinal injection needle [17] and for low back pain injections [18]. In addition, remote center of motion mechanisms has been explored for microwave therapy of liver tumors [19] and shoulder arthrography [20]. The minimally invasive robotics in an MRI environment is a system comprising of 9-DoF parallel robot, designed for needle-based prostate cancer treatments [21]. While piezoelectric motors can provide high accuracy actuation, RF interference between the motor current and the MRI field necessitates pausing the motor's operation throughout the imaging process [22].

Another method of actuation employed in the MR environment is pneumatics. This form of actuation is beneficial as they can be designed to have minimal effect on the MR image quality. In addition, the operation principle relies on compressed air, and so MR-conditional robots using pneumatics can be seamlessly integrated with the air infrastructure existing in hospitals. Several custom designed pneumatic motors have been developed and implemented in MR-guided robots for prostate cancer procedures [5, 23], intracerebral hemorrhage evacuation [13], and breast biopsy [14]. Pneumatic cylinders are another type of actuator that have been used to drive MR-conditional robots. Fischer *et al.* demonstrated a pneumatic robot for prostate cancer diagnosis and treatment [24]. Yang *et al.* created a 1-DoF pneumatic robot for conducting breast biopsies [25]. A 4-DoF robot was developed by Franco and Ristic for the placement of needles in MR-guided liver cancer ablation [26]. A 5-DoF, pneumatic cylinder-based, active cannula robot was created by Comber *et al.* for neuro-surgical purposes [27]. INNOMOTION, a commercially available, pneumatically driven robot is currently being used for MR-guided sciatic pain therapy, biopsies, and drainage [28].

The works mentioned previously are all cases of motion devices designed for very specific tasks in the MR environment. The concept of a general purpose motion device on the other hand is scarce in MR-conditional robotics, but is ubiquitous in the field of industrial robotics. For example, in manufacturing, a single robot can be used for a multitude of tasks such as assembly, material handling, packaging, etc. With precise and accurate enough motions this concept could also be applied to the medical robotics community. Few MR-conditional devices have been proposed for general purpose motion generation. Tsekos *et al.* developed a 7-DoF MR-Compatible robotic system designed for a variety minimally invasive interventions [29]. The main focus of this work however is solely minimally invasive interventions and so the structure of the device is not suitable for general motion creation. Christoforou *et al.* presented a 5-DoF manually operated robotic manipulation system for minimally invasive interventions [30]. The primary pitfalls of this work are that it does not enable autonomous actuation and lacks a sixth DoF for full spatial motion generation. Hungr *et al.* developed a 5-DoF CT-and MRI-guided robot for percutaneous needle interventions [31]. Similar to the previous systems, while designed to be general enough to be applied to a variety of needle interventions, the system lacks DoF for full spatial motion generation.

This paper investigates the design, fabrication, and characterization of a parallel robot for generalized motion in the MR environment. The motivation of this work is to create a robot capable of providing accurate 6-DoF motion for both motion modeling and developing future interventional platforms [32]. The work presented in this paper is an extension of our previous work [33], with the addition of in scanner evaluation and performance. The remainder of this paper is arranged as follows. Section 2 presents the design, kinematics, and workspace analysis of the robot. The low-level control used on the robotic system is described in Sec. 3. Section 4 presents the experimental results of benchtop characterization tests and MRI scanner motion experiments, while the final discussion and conclusion are given in Sec. 5.

2. Robot Design and Kinematics

2.1. Robot hardware design

The proposed MR-conditional robot is based on the traditional Stewart–Gough platform [34, 35]. This robotic structure has been used in a wide variety of applications including motion simulators, vibration isolation, manipulation, etc. [36]. To the authors' knowledge, this popular kinematic structure has yet to make its way into the MR environment with the exception of one study that presents a fully three-dimensional (3D) printed multi-level Stewart–Gough platform for MRI applications [37]. This work however focuses strictly on the fabrication techniques and presents no demonstration of the device's functionality.

In this work, the robot's structure is made of three primary components: (1) a lower, fixed base, (2) an upper, moving platform, and (3) six identical limbs linking the base and platform to each other. The limbs are comprised of a purely prismatic joint ($\boldsymbol{P}$) that is linked to the lower base through universal joints ($\boldsymbol{U}$) and the moving platform through spherical joints ($\boldsymbol{S}$). The robot configuration is shown in Fig. 1. By changing the limb lengths, the moving platform's pose can be achieved. This parallel robot configuration provides a high load-to-weight ratio, high rigidity and robustness against error accumulation [38]. Figures 1(a) and 1(b) depict the robot in both the homed and fully extended configurations, respectively.

2.2. Robot fabrication

Robot fabrication materials were carefully selected to provide MRI compatibility. Laser cut acrylic sheets were used to make the base and moving platforms. Custom universal joints and spherical joints were designed and printed on a high resolution stereolithography 3D printer using the photopolymer material Tough 2000 (T020-01, Formlabs, USA). The active prismatic joint, utilizes a double-acting MR-conditional pneumatic cylinder (Airpel E9, Airpot Co.). The pneumatic cylinder includes a glass cylinder bore, graphite piston, rubber seals, and a plastic housing. The only metallic components on the actuator are the brass piston–rod but this has been demonstrated in other studies to have minimal effect on the image quality [39]. The piston–rod of the pneumatic cylinder can freely rotate about its central axis resulting in a cylindrical joint rather than prismatic. This redundant DoF is negated by incorporating a second brass rod in parallel with piston–rod, with a 3D printed bracket that houses a bushing to ensure the smooth movement of the secondary rod. The piston–rod and the secondary rod are then coupled together to create the necessary prismatic joint.

To enable joint space feedback, each pneumatic cylinder was fitted with a 500 lines per inch optical encoder (EM1, US-Digital) and a linear transmissive strip was fixed to the secondary rod. The pneumatic cylinders are controlled by two proportional pressure regulators (ITV1031-21N2BL4, SMC Corporation) with built-in pressure sensors. This configuration enables direct control of the pressure to each chamber of the cylinders. The proportional regulators are not MRI compatible, and so 10 m long (inner diameter = 3.175 mm) transmission tubes were used. The control algorithms were created on a Simulink xPC target machine. An analog output board (PCI-DAC6703, National Instruments) provided a 16-bit control voltage (0–5 V) to the pressure regulators in the operating output range of 0–50 psi. The encoder data was measured using a 32-bit encoder counter PCI (CNT32-8M, Contec) at a sampling rate of 1 kHz.

2.3. Inverse kinematics analysis

The robot's geometry can be described by assigning coordinate frames to both the fixed base and the moving platform as seen in Fig. 1(a). The fixed frame, B, of the robot is assigned at the point O_B on the base and similarly, the moving frame, P, of the robot is assigned at the point O_P on the moving platform. The position where the passive joints are attached in the frames B and P can be expressed as

$$ {}^{P}\mathbf{p}_i = r_P[\cos(\gamma_i)\ \sin(\gamma_i)\ 0]^T, \tag{1}$$

$$ {}^{B}\mathbf{b}_i = r_B[\cos(\Gamma_i)\ \sin(\Gamma_i)\ 0]^T, \tag{2}$$

$$ \Gamma_i = \frac{(i-1)\pi}{3} - \alpha_B;\ \gamma_i = \frac{(i-1)\pi}{3} - \alpha_P, \quad \text{for } i = 1, 3, 5, \tag{3}$$

$$ \Gamma_i = \Gamma_{i-1} + 2\alpha_B;\ \gamma_i = \gamma_{i-1} + 2\alpha_B, \ \ \text{for } i = 2, 4, 6, \tag{4}$$

where r_B and r_P are the radii of the base and moving platform, respectively, and α_B and α_P are half the angle between the base and platform joint attachment points, respectively, as shown in Fig. 1(c).

The inverse kinematics of the robot uses the desired platform pose to calculate the limb lengths required to achieve that pose. The vector diagram for the ith limb used to solve the inverse kinematics can be seen in Fig. 2. The position vector of the moving platform defined in the fixed frame is given by

$$ {}^{B}\mathbf{d} = [x\ \ y\ \ z]^T. \tag{5}$$

The three Euler angles: Roll (ϕ), Pitch (θ), and Yaw (ψ) are used to describe the orientation of the platform. The vector loop closure equation for the ith limb is then given by

$$ \mathbf{l}_i = {}^{B}\mathbf{d} + {}^{B}R_P \cdot {}^{P}\mathbf{p}_i - {}^{B}\mathbf{b}_i, \tag{6}$$

where ${}^{B}R_P$ is a rotation matrix describing the orientation of the moving platform in the base frame. This rotation matrix is given by

$$ {}^{B}R_P \quad = R_z(\psi)R_y(\theta)R_x(\phi), \tag{7}$$

$$ R_z(\psi) = \begin{bmatrix} \cos\psi & -\sin\psi & 0 \\ \sin\psi & \cos\psi & 0 \\ 0 & 0 & 1 \end{bmatrix}, \tag{8}$$

$$R_y(\theta) = \begin{bmatrix} \cos\theta & 0 & \sin\theta \\ 0 & 1 & 0 \\ -\sin\theta & 0 & \cos\theta \end{bmatrix}, \tag{9}$$

$$R_x(\phi) = \begin{bmatrix} 1 & 0 & 0 \\ 0 & \cos\phi & -\sin\phi \\ 0 & \sin\phi & \cos\phi \end{bmatrix}. \tag{10}$$

The length of the ith limb can then be found by taking the Euclidean norm of the limb vector in (6)

$$l_i = \left\| {}^B\mathbf{d} + {}^B R_P \cdot {}^P\mathbf{p}_i - {}^B\mathbf{b}_i \right\|. \tag{11}$$

2.4. Jacobian analysis

The Jacobian matrix, J, gives a relationship between the limb velocities and the twist of robot end-effector. This relationship is given by

$$\dot{\mathbf{L}} = J\dot{\mathbf{X}}, \tag{12}$$

$$\dot{\mathbf{L}} = \left[\dot{l}_1 \ \dot{l}_2 \ \dot{l}_3 \ \dot{l}_4 \ \dot{l}_5 \ \dot{l}_6\right]^T, \tag{13}$$

$$\dot{\mathbf{X}} = \left[\dot{x} \ \dot{y} \ \dot{z} \ \dot{\phi} \ \dot{\theta} \ \dot{\psi}\right]^T. \tag{14}$$

The Jacobian matrix can be found from the velocity loop closure equation for each limb as outlined in [40]. This is done by first taking the time derivative of the vector loop closure (6)

$$\dot{l}_i {}^B\hat{\mathbf{s}}_i + l_i {}^B\dot{\hat{\mathbf{s}}}_i = {}^B\mathbf{v}_P + {}^B\dot{R}_P \cdot {}^P\mathbf{p}_i + {}^B R_P \cdot {}^P\dot{\mathbf{p}}_i + {}^B\dot{\boldsymbol{b}}_i, \tag{15}$$

where ${}^B\mathbf{v}_P$ is the moving platform’s velocity at point O_P, and $\hat{\boldsymbol{s}}_i$ is a unit vector in the direction of limb i. The time derivative of this unit vector is given as

$$l_i {}^B\hat{\mathbf{s}}_i = l_i\left({}^B\omega_i \times \hat{\mathbf{s}}_i\right), \tag{16}$$

where ${}^B\omega_i$ is the angular velocity of limb i relative to the fixed frame. Additionally, ${}^B\dot{R}_P \cdot {}^P\mathbf{p}_i$ is given by

$${}^B\dot{R}_P \cdot {}^P\mathbf{p}_i = {}^B\omega \times {}^B\mathbf{b}_i. \tag{17}$$

Since the time derivative of vector $\mathbf{p}_i$ in the moving frame is zero and the derivative of the vector $\mathbf{b}_i$ in the base frame is zero, the velocity loop closure can be simplified to

$$\dot{l}_i {}^B\hat{\mathbf{s}}_i + l_i\left({}^B\omega_i \times \hat{\mathbf{s}}_i\right) = {}^B\mathbf{v}_P + {}^B\omega \times {}^B\mathbf{b}_i\,. \tag{18}$$

The passive joint rate ${}^B\omega_i$ can then be eliminated using dot multiplication of (18) with $\hat{\mathbf{s}}_i$ giving

$$\dot{l}_i = \hat{\mathbf{s}}_i \cdot \mathbf{v}_P + \left(\mathbf{p}_i \times \hat{\mathbf{s}}\right)_i \omega\,. \tag{19}$$

The Jacobian matrix is then a 6 × 6 square matrix given by

$$\boldsymbol{J} = \begin{bmatrix} \hat{\mathbf{s}}_1^T & \left(\mathbf{p}_1 \times \hat{\mathbf{s}}_1\right)^T \\ \hat{\mathbf{s}}_2^T & \left(\mathbf{p}_2 \times \hat{\mathbf{s}}_2\right)^T \\ \vdots & \vdots \\ \hat{\mathbf{s}}_6^T & \left(\mathbf{p}_6 \times \hat{\mathbf{s}}_6\right)^T \end{bmatrix}. \tag{20}$$

2.5. Forward kinematics analysis

The forward kinematics of the robot enables for the computation of the platform's pose given desired limb lengths. Finding a solution to the forward kinematics is challenging as there are no closed-form solutions to the vector loop closure (11) which is comprised of six highly nonlinear equations. Therefore, the Newton–Raphson iterative numerical method can be implemented for parallel robot forward kinematics [41]. Given the desired limb lengths l_i, the objective is to calculate the estimated lengths l_i^* on an iterative process given an initial pose estimate $\mathbf{X}_{\mathbf{j}-1}$. The estimated limb lengths l_i^* are then solved for using (11) and the value of $\mathbf{X}_{\mathbf{j}-1}$ is incremented by a small step-size until the scalar function $f_i(\mathbf{X}) = l_i - l_i^*$ is minimized.

A Jacobian-based control scheme, known as resolved-rate motion control [42], was then implemented for the task space control of the robot. The control scheme directly compares a desired task space pose, $\mathbf{X}_d$, with the current task space pose of the robot, $\mathbf{X}_i$, calculated by the forward kinematics using the actual leg positions from the linear encoder feedback.

$$l_i = l_{i-1} + \boldsymbol{J}\alpha\left(\mathbf{X}_d - \mathbf{X}_i\right), \tag{21}$$

where α is a positive scaling factor.

2.6. Workspace analysis

The robot is designed to operate in the restricted space of a closed bore MRI scanner and so a workspace analysis was performed to evaluate the working range of the robot. The analysis was done using the inverse kinematics developed in Sec. 2.3 as a result of its computational simplicity. A 3D scanning volume is first generated then (11) is used to verify if discrete points in the scanning volume are reachable by the robot under the following joint constraints:

$$l_{\min} < l_i < l_{\max}, \tag{22}$$

where $l_{\min} = 0$ mm and $l_{\max} = 75$ mm. Additionally, constraints are added to ensure the passive joints do not exceed their physical limits (for both the U and S joints: $\theta_{\max} = 40°$). For points that are reachable by the robot, their coordinates are saved and any points unreachable by the robot are discarded. This results in a point cloud making up the workspace of the robot. The complete workspace representation of the robot would exist in six-dimensional space (3-DoF position and 3-DoF orientation). However, the 3D positional workspace with constant orientation is reported in this paper to simplify the representation (see Figs. 3(a)–3(c) for the results). The volume of the robot's workspace was found to be 1016 cm^3.

A potential application of this device is for image-guided minimally invasive interventions such as radio-frequency ablation cancer treatment of abdominal organs [43]. In the dynamic region of the abdomen, some of the largest displacements that occur are in the cranio-caudal direction for the pancreas and liver with 23.7 ± 15.9 mm and 24.4 ± 16.4 mm, respectively, during normal respiration [44], however, this can increase to 43 mm and 55 mm, respectively, during maximum respiration or deep breathing [45]. Robots designed for this procedure should be able to cover this range of motions. From the workspace analysis, it can be seen that this motion range is achievable by the robot along either the x- or y-axis. Additionally, the volume of the workspace is compared to the average volume of some major organs that are typically the focus of minimally invasive needle insertion procedures, namely, the liver, spleen, kidneys, and pancreas. The volumes reported are the average volumes of the organs for an adult male human since they represent the mean upper bound on the volume [46]. In the case of the spleen, kidneys, and pancreas, it can be seen that the robot's workspace volume is significantly greater and so is able to encompass 100% of the organ's volume. In the case of the liver, the robot is only capable of covering 60% of its volume. However, it should be noted that the robot is body mounted and so can be placed in any position the clinician deems necessary to reach desired targets.

3. Robot Low-Level Control

3.1. Pneumatic system model

The pneumatic circuit diagram can be seen in Fig. 4. Using this, the model for a double-acting pneumatic cylinder dynamics is given by

$$P_a A_a - P_b A_b - F_{\text{friction}} = m\ddot{x}, \tag{23}$$

where P_a is the pressure to chamber A, A_a is the cross-sectional area of chamber A, P_b is the pressure to chamber B, A_b is the cross-sectional area of chamber B and m is the combined mass of the piston and rod. The friction term, F_{friction}, is described by viscous and Coulomb frictional forces. The friction model is given by

$$F_{\text{friction}} = \mu_v \dot{x} + \mu_c \operatorname{sign}(\dot{x}), \tag{24}$$

where the terms μ_v and μ_c are the coefficients of the viscous and Coulomb friction, respectively. With the pressure to both chambers of the pneumatic cylinder being directly controlled by the proportional regulators, the chamber dynamics and mass flow dynamics can be neglected. This results in a reduced order model that can be used to simplify the control problem.

3.2. Sliding mode controller

Taking into consideration inconsistencies and uncertainties in the model, it is preferable to implement a robust control system to solve the nonlinear control problem [47]. Inspired by the work done by Wang *et al.* in [48], a sliding mode controller (SMC) is used to control the pneumatic cylinder because the controller can account for model inconsistencies and the delay induced by the 10 m pneumatic tubing. For development of the control law U, the sliding surface, S, is first defined by

$$S = \lambda e + \dot{e}, \tag{25}$$

where the e is the error given by $e = x_d - x$, and λ is strictly positive. In order to guarantee stable error dynamics, $S\dot{S} \leq 0$ must be enforced. The control law can then be written as

$$U = u_{\mathrm{eq}} + u_{\mathrm{sat}}, \tag{26}$$

where u_{eq} allows the system's dynamics to be maintained on the sliding surface $S = 0$. This term can be calculated by taking the derivative of (25) and substituting into (23).

$$u_{\mathrm{eq}} = m(\ddot{x}_d + \lambda \dot{x}_d) + \dot{x}(\mu_v - \lambda m) + \mu_c \mathrm{sign}(\dot{x}). \tag{27}$$

In (26) u_{sat} is a saturation function that compensates for uncertainty in the model when the state leaves the sliding surface. The saturation function is given by

$$u_{\mathrm{sat}} = k \times \mathrm{sat}\left(\frac{S}{d}\right) = \begin{cases} k \times \mathrm{sign}\left(\frac{S}{d}\right), & |S| \geq d, \\ k \times \left(\frac{S}{d}\right), & |S| < d, \end{cases} \tag{28}$$

where the constants λ, k, and d are tuned until the desired performance of the system is achieved. Because of the low friction between the piston and the glass cylinder bore, as well as the low stiffness of actuators used, external damping was required to reduce system overshoot. This was accomplished by increasing the Coulomb friction acting on the pneumatic actuator's piston–rod.

4. Experiments and Results

4.1. Pneumatic cylinder control

In this section, the performance of the SMC designed in Sec. 3.2 is evaluated. The algorithm was initially tested by applying a 25 mm step input to the system. For each test, the pneumatic cylinder was vertically mounted using a 3D printed bracket. To demonstrate the controller's robustness, several external weights ranging from 20 g to 200 g were added to the pneumatic cylinder and the performance was compared to the scenario with no external loading. The experiments were repeated three times for a total of 15 trials. The average steady-state error across all trials was 0.69 ± 0.14 mm, with the smallest recorded error of 0.24 mm observed in the no loading scenario and the largest recorded error of 0.95 mm seen in the 200 g loading scenario. Figure 5(a) shows a comparison of the step responses. In all scenarios, no overshoot of the actuator was observed. Furthermore, the time delay of 0.352 s introduced by the 10 m long transmission tubes can be seen in the initial difference between the input signal and the recorded encoder data. The delay can be reduced by using MR-conditional piezoelectric valves such that part of the control electronics can be placed inside the scanner to reduce the air hose length [49].

In addition to the step response, the SMC was given a sinusoidal target signal $x = 20\sin\left(\frac{\pi t}{10}\right) + 25$ to examine the pneumatic cylinder's dynamic tracking capabilities. The result of the experiment is shown in Fig. 5(b) where it can be seen that the actuator closely tracks the input sinusoidal signal with an average error of 0.67 ± 0.40 mm.

4.2. Robot targeting accuracy

As previously mentioned, a potential application of the robot is for image-guided percutaneous needle interventions [43]. In this scenario, the robot would be mounted to the patient's body using adjustable straps and commanded to automatically guide a needle to a desired target under intraoperative image guidance. A CAD rendering of this scenario can be seen in Fig. 6(a). A benchtop experiment was performed to demonstrate the potential of applying the parallel robot for active needle insertions. An agar-agar phantom was used in the experiment to simulate human tissue. The tip of an 18-gauge needle was fitted with a 6-DoF EM sensor before being mounted perpendicular to the robot end-effector as seen in Fig. 6(b). The needle pose was recorded using an EM tracking system (Aurora, NDI Medical, Ontario Canada) and located in the robot reference frame using point-based coordinate registration [13]. Five targets in the phantom were chosen at increasing insertion depths and sent to the robot's task space control system. An access hole in the base of the robot with diameter of 30 mm allowed the needle to pass through and directly access three of the targets; however, the other two targets were located outside of this access hole requiring the moving platform to be oriented at an angle of 10° about the the x-axis and y-axis in each of the cases.

The results of the targeting experiment are shown in Fig. 6(c), where the red markers represent the desired target and the blue markers represent the needle tip location as recorded by the EM tracker. The position error is calculated by the Euclidean distance between the desired and measured positions. Each desired goal was targeted three times for a total of 15 trials. The average position error was found to be 1.20 ± 0.43 mm and the average deviation from the desired needle orientation was 1.09 ± 0.57°.

4.3. MRI compatibility evaluation

All MRI experiments were conducted in a 3T Philips Ingenia Elition X whole body MRI scanner. MRI compatibility of the robot was evaluated by quantifying the variation in signal-to-noise ratio (SNR) within a region of interest (ROI) caused by the presence of the robot. 3D gradient recalled echo (GRE) images of a $CuSO_4$ phantom bottle were taken under three different scenarios: (1) without the robot (as a control), (2) with the robot powered off, and (3) with the robot powered on. In the latter two scenarios, the phantom bottle was placed in contact with the base of the robot. The images of the phantom bottle can be seen in Fig. 7(a) where qualitatively there is no apparent change in the image contrast, and no obvious image artifacts were created to the presence and operation of the robot. The SNR in a 30 × 30 pixel ROI was calculated by

$$\mathrm{SNR} = \frac{\mu_1}{\sigma_1}, \tag{29}$$

where μ_1 is the mean signal in the ROI and σ_2 is the standard deviation of a 30 × 30 pixel ROI taken in the noise background of the image. The normalized SNR of the MR images corresponding to each scenario is shown in Fig. 7(b). The maximum variation in SNR observed was 4.73%.

4.4. Robot motion experiment

One of the primary proposed applications of this robotic platform is accurate motion generation for MRI motion modeling. To demonstrate the feasibility of this, motion studies were conducted in the MRI scanner. As seen in Fig. 8(a), a 3D printed phantom box was mounted to the moving platform of the robot and filled with ultrasound coupling gel to indicate the envisioned application for motion compensation. The robot was commanded to move the phantom under three scenarios: (1) pure translation, (2) pure rotation, and (3) combined translation and rotation. Note that the position and orientation of the end-effector were calculated based on three fiducial markers mounted on the end-effector to simply the calculation process. In each case, 3D GRE scans of the fiducial markers were acquired and uploaded to 3D Slicer (www.slicer.org), where the end-effector's location in the MRI coordinate frame could be obtained. The robot was registered to the MRI coordinate frame using point-based registration [13], which is given by the following equation:

$$P_{\mathrm{robot}} = R^{*}P_{\mathrm{MRI}} + t, \tag{30}$$

where P_{robot} is the position of fiducial markers in the robot coordinate frame, P_{MRI} is the corresponding fiducial marker position in the MRI frame, R is a rotation matrix, and t is a translation matrix. The fiducial marker registration error (FRE) is given by

$$\mathrm{FRE} = \sqrt{\frac{1}{n}\sum_{i=1}^{n}\left|R^{*}P_{\mathrm{MRI}_i} + t - P_{\mathrm{robot}\,i}\right|^{2}}, \tag{31}$$

where n is the number of fiducial markers. In this case, three fiducial markers (PinPoint, Beekley Medical) are used for the image registration. For these experiments, the FRE was 1.2 mm.

In the first experiment designed to evaluate pure translations, the robot was commanded to move the end-effector in a point-to-point fashion for nine different locations in the XY-plane while a constant Z-height of 20 mm and a constant orientation (no rotation around each axis) was maintained. A top view of this motion experiment can be seen in Fig. 8(b) where the red markers represent the desired end-effector position, the blue markers represent the measured position from MRI images, and the green markers indicate the position of the moving platform calculated offline using the forward kinematics and the recorded encoder data. The error is defined as the Euclidean distance between the measured end-effector position and the desired end-effector position. The mean positional error was found to be 1.68 ± 0.31 mm.

In the second experiment designed to evaluate rotations, the robot was commanded to orient the end-effector about each the $x-$, $y-$, and z-axes with ±5° angulation. A constant Z-height of 20 mm and no translation commands were given to the robot. The result of the rotation experiment can be seen in Table 2. The mean orientational error was found to be 1.51 ± 0.32°. In both the first and second experiments, the robot was able to successfully maintain its desired position in the Z-axis with a mean error of 0.69 ± 0.53 mm.

Lastly, a final experiment was conducted where a mixture of translations and rotations were given to the robot to test its ability to perform full 6-DoF motion. The robot was first commanded to move to arbitrary positions along the $x-$, $y-$, and z-axes. Then arbitrary rotation commands were given to the robot. This was done for three trials and the average positional error was found to be 2.10 ± 0.35 mm and the average orientational error was found to be 1.67 ± 0.32°.

5. Discussion and Conclusion

In this paper, the design, analysis, and preliminary characterization of a general purpose 6-DoF parallel robotic motion platform for MRI applications were presented. The robot is designed based on a standard Stewart–Gough platform and is powered by six pneumatic cylinder actuators. The robot's design, fabrication, kinematics, and workspace analysis were presented. This was followed by a description of the SMC for the robot's joint space control. Experiments were then carried out to evaluate both the pneumatic actuator controller and the high-level control of the robotic system.

Pneumatic actuator tracking experiments demonstrated that the SMC is robust enough to account for changes in system uncertainties such as increased weight on the actuator, with the mean error across 15 experiments being 0.69 ± 0.14 mm in response to a step input. The mean error in response to a sinusoidal input was determined to be 0.67 ± 0.40 mm. These errors can primarily be attributed to the manual tuning of the SMC parameters. This can be reduced in future iterations by using an adaptive control strategy in conjunction with the SMC.

To demonstrate one potential application of this device, a benchtop phantom targeting experiment was performed. In this experiment, the robot was commanded to drive a needle to five different targets of differing depths and orientations. The average position error at the needle tip was 1.20 ± 0.43 mm, while the average orientation error was 1.09 ± 0.57°. The differences between the measured tip pose and the target may be attributed to manufacturing tolerances in the robot, particularly, the custom designed needle that was mounted to the robot moving platform.

The robot’s compatibility in the MRI environment was evaluated and indicated that the robot could operate safety inside a 3T MRI scanner with no obvious artifacts being created in the image ROI. Additionally, the robot was shown to have minimal effect on the SNR with the largest recorded variation being 4.7%. Lastly, the robot’s performance was evaluated in the MR environment by conducting up to 6-DoF motion experiments. Three experiments were conducted with the robot being commanded to move the end-effector with pure translation (positional error = 1.68 ± 0.31 mm), pure rotation (orientational error = 1.51 ± 0.32°), and finally a combination of both translation and rotation (positional error = 2.10 ± 0.35 mm and orientational error = 1.67 ± 0.32°). The primary contributor to these errors is likely the MRI-robot registration error.

While the robot has shown promising results in both the benchtop environment and inside the MRI scanner, more work must be done to create a more robust and reliable system. Our future work will include optimization of the design to fit more closely to the tight restrictions of the MRI bore and utilizing higher quality machined components. Additionally, our work as presented in this study presents the kinematic formulation of this robot, however, the intent is to include dynamic force control for safety purposes, especially if the robot is to perform operations with humans. Lastly, with dynamic control, we will be able to extend the motion generation capabilities of the robot beyond just point-to-point motions and simulate more complicated motion profiles. This will enable rapid testing of motion compensation image sequences without the need for human subjects which is time intensive and limited in availability.

Acknowledgments

This work was supported in part by funding from NIBIB R21EB025258.

Biographies

Mishek Musa received B.S. degree in Mechanical Engineering from the University of Arkansas, Fayetteville, AR, USA, in 2019, and M.S. degree in Mechanical Engineering from the University of Arkansas, Fayetteville, AR, USA, in 2021. He is currently pursuing Ph.D. degree in Mechanical Engineering from the University of Arkansas, Fayetteville, AR, USA. His research interests include robotics, mechatronic systems, and control system design.

Saikat Sengupta received B.S. in Electrical Engineering from the Veermata Jijabai Technical Institute, Mumbai, India, in 2000, M.Sc. in Biomedical Engineering from the University of Memphis, Memphis, TN, USA, in 2002, and Ph.D. in Biomedical Engineering, the Vanderbilt University, Nashville, TN, USA, in 2010. He is Research Assistant Professor at the Vanderbilt University Institute of Imaging Science, Nashville, TN, USA. His current research interests include high field MRI, interventional MRI, and motion correction.

Yue Chen received B.S. in Vehicle Engineering from the Hunan University, Hunan, China, in 2010, M.Phil. in Mechanical Engineering from the Hong Kong Polytechnic University, Hung Hom, Hong Kong, in 2013, and Ph.D. in Mechanical Engineering, the Vanderbilt University, Nashville, TN, USA, in 2018. He is Assistant Professor in the Department of Biomedical Engineering, the Georgia Institute of Technology, Atlanta, GA, USA. His current research interests include medical robotics and soft robots.

References

1. Xiao Q, Monfaredi R, Musa M, Cleary K and Chen Y, MR-conditional actuations: A review, Ann. Biomed. Eng 48(12) (2020) 2707–2733. [PubMed: 32856179]
2. Musa M, Sengupta S and Chen Y, MRI-compatible soft robotic sensing pad for head motion detection, IEEE Robot. Autom. Lett 7(2) (2022) 3632–3639.
3. Sengupta S, Tadanki S, Gore JC and Welch EB, Prospective realtime head motion correction using inductively coupled wireless NMR probes, Magn. Reson. Med 72(4) (2014) 971–985. [PubMed: 24243810]
4. Stoianovici D, Kim C, Srimathveeravalli G, Sebrecht P, Petrisor D, Coleman J, Solomon SB and Hricak H, MRI-safe robot for endorectal prostate biopsy, IEEE/ASME Trans. Mechatronics 19(4) (2013) 1289–1299. [PubMed: 25378897]
5. Chen Y, Xu S, Squires A, Seifabadi R, Turkbey IB, Pinto PA, Choyke P, Wood B and Tse ZTH, MRI-guided robotically assisted focal laser ablation of the prostate using canine cadavers, IEEE Trans. Biomed. Eng 65(7) (2017) 1434–1442. [PubMed: 28961099]
6. Gunderman A, Schmidt E, Morcos M, Tokuda J, Seethamraju RT, Halperin H, Viswanathan A and Chen Y, MR-tracked deflectable stylet for gynecologic brachytherapy, IEEE/ASME Trans. Mechatronics 27 (2021) 407–417. [PubMed: 35185321]
7. Nofiele J, Yuan Q, Kazem M, Tatebe K, Torres Q, Sawant A, Pedrosa I and Chopra R, An MRI-compatible platform for onedimensional motion management studies in MRI, Magn. Reson. Med 76(2) (2015) 702–712. [PubMed: 26493684]
8. Quasar™ MRI^{4D} motion phantom (2021).
9. Zeus: MRgRT motion management QA phantom (2021).

10. MRI-compatible linear motion stage.
11. Chen Y, Wang W, Schmidt EJ, Kwok K-W, Viswanathan AN, Cormack R and Tse ZTH, Design and fabrication of MR-tracked metallic stylet for gynecologic brachytherapy, IEEE/ASME Trans. Mechatronics 21(2) (2016) 956–962. [PubMed: 28989272]
12. Chen Y, Poorman ME, Comber DB, Pitt EB, Liu C, Godage IS, Yu H, Grissom WA, Barth EJ and Webster RJ III, Treating epilepsy via thermal ablation: Initial experiments with an MRI-guided concentric tube robot, in Proc. 2017 Design of Medical Devices Conf (ASME, 2017).
13. Chen Y, Godage IS, Sengupta S, Liu CL, Weaver KD and Barth EJ, MR-conditional steerable needle robot for intracerebral hemorrhage removal, Int. J. Comput. Assist. Radiol. Surg 14(1) (2019) 105–115. [PubMed: 30173334]
14. Groenhuis V, Siepel FJ, Veltman J, van Zandwijk JK and Stramigioli S, Stormram 4: An MR safe robotic system for breast biopsy, Ann. Biomed. Eng 46(10) (2018) 1686–1696. [PubMed: 29786775]
15. Elhawary H, Tse ZT, Hamed A, Rea M, Davies BL and Lamperth MU, The case for MR-compatible robotics: A review of the state of the art, Int. J. Med. Robot 4(2) (2008) 105–113. [PubMed: 18481822]
16. US Food and Drug Administration, Establishing safety and compatibility of passive implants in the magnetic resonance (MR) environment, US Food and Drug Administration, Silver Spring (2014).
17. Meinhold W, Martinez DE, Oshinski J, Hu AP and Ueda J, A direct drive parallel plane piezoelectric needle positioning robot for MRI guided intraspinal injection, IEEE Trans. Biomed. Eng 68(3) (2021) 807–814 [PubMed: 32870782]
18. Li G, Patel NA, Liu W, Wu D, Sharma K, Cleary K, Fritz J and Iordachita I, A fully actuated body-mounted robotic assistant for MRI-guided low back pain injection, in 2020 IEEE Int. Conf. Robotics and Automation (ICRA) (IEEE, 2020), pp. 5495–5501.
19. Hata N, Hashimoto R, Tokuda J and Morikawa S, Needle guiding robot for MR-guided microwave thermotherapy of liver tumor using motorized remote-center-of-motion constraint, in Proc. IEEE Int. Conf. Robotics and Automation (IEEE, 2005), pp. 1652–1656.
20. Monfaredi R, Seifabadi R, Iordachita I, Sze R, Safdar NM, Sharma K, Fricke S, Krieger A and Cleary K, A prototype body-mounted MRI-compatible robot for needle guidance in shoulder arthrography, in Proc. IEEE/RAS-EMBS Int. Conf. Biomedical Robotics and Biomechatronics (IEEE, 2014), pp. 40–45.
21. Moreira P, van de Steeg G, Krabben T, Zandman J, Hekman EEG, van der Heijden F, Borra R and Misra S, The MIRIAM robot: A novel robotic system for MR-guided needle insertion in the prostate, J. Med. Robot. Res 02(04) (2016) 1750006.
22. Wendt O, Oellinger J, Lüth TC, Felix R and Boenick U, The effects of the use of piezoelectric motors in a 1.5-tesla high-field magnetic resonance imaging system (MRI), Biomed. Tech 45(1–2) (2000) 20–25.
23. Stoianovici D, Song D, Petrisor D, Ursu D, Mazilu D, Muntener M, Schar M and Patriciu A, “MRI stealth” robot for prostate interventions, Minim. Invasive Ther. Allied Technol 16(4) (2007) 241–248. [PubMed: 17763098]
24. Fischer GS, Iordachita I, Csoma C, Tokuda J, DiMaio SP, Tempany CM, Hata N and Fichtinger G, MRI-compatible pneumatic robot for transperineal prostate needle placement, IEEE/ASME Trans. Mechatronics 13(3) (2008) 295–305. [PubMed: 21057608]
25. Yang B, Tan UX, McMillan AB, Gullapalli R and Desai JP, Design and control of a 1-DOF MRI-compatible pneumatically actuated robot with long transmission lines, IEEE/ASME Trans. Mechatronics 16(6) (2011) 1040–1048. [PubMed: 22058649]
26. Franco E and Ristic M, Design and control of needle positioner for MRI-guided laser ablation of the liver, in 2014 IEEE/ASME 10th Int. Conf. Mechatronic and Embedded Systems and Applications (MESA) (IEEE, 2014), pp. 1–6.
27. Comber DB, Barth EJ and Webster RJ, Design and control of an magnetic resonance compatible precision pneumatic active cannula robot, J. Med. Dev 8(1) (2013) 011003.
28. Melzer A, Gutmann B, Remmele T, Wolf R, Lukoscheck A, Bock M, Bardenheuer H and Fischer H, Innomotion for percutaneous image-guided interventions, IEEE Eng. Med. Biol. Mag 27(3) (2008) 66–73.

29. Tsekos NV, Christoforou E and Ozcan A, A general-purpose MR-compatible robotic system, IEEE Eng. Med. Biol. Mag 27(3) (2008) 51–58. [PubMed: 18519182]
30. Christoforou EG, Seimenis I, Andreou E, Eracleous E and Tsekos NV, A novel, general-purpose, MR-compatible, manually actuated robotic manipulation system for minimally invasive interventions under direct MRI guidance, Int. J. Med. Robot. Comput. Assist. Surg 10(1) (2014) 22–34.
31. Hungr N, Bricault I, Cinquin P and Fouard C, Design and validation of a CT- and MRI-guided robot for percutaneous needle procedures, IEEE Trans. Robot 32(4) (2016) 973–987.
32. Clifford MA, Banovac F, Levy E and Cleary K, Assessment of hepatic motion secondary to respiration for computer assisted interventions, Comput. Aided Surg 7(5) (2002) 291–299. [PubMed: 12582982]
33. Musa M, Sengupta S and Chen Y, Design of a 6 DOF parallel robot for MRI-guided interventions, in 2021 Int. Symp. Medical Robotics (ISMR) (IEEE, 2021), pp. 1–7.
34. Gough VE and Whitehall SG, Universal tyre test machine, in Proc. 9th Int. Technical Congress, Fisita (Institution of Mechanical Engineers, 1962), pp. 117–137.
35. Stewart D, A platform with six degrees of freedom, Proc. Inst. Mech. Eng 180 (1965) 371–386.
36. Dasgupta B and Mruthyunjaya T, The Stewart platform manipulator: A review, Mech. Mach. Theory 35(1) (2000) 15–40.
37. Slightam JE and Gervasi VR, Novel integrated fluid-power actuators for functional end-use components and systems via selective laser sintering nylon 12, in 2012 Int. Solid Freeform Fabrication Symp (University of Texas at Austin, 2012), pp. 197–211.
38. Ghobakhloo A, Eghtesad M and Azadi M, Adaptive-robust control of the Stewart–Gough platform as a six DOF parallel robot, in 2006 World Automation Congress (IEEE, 2006), pp. 1–6.
39. Fischer GS, Krieger A, Iordachita I, Csoma C, Whitcomb LL and Fichtinger G, MRI compatibility of robot actuation techniques – A comparative study, Med. Image Comput. Comput. Assist. Interv 11 (Pt 2) (2008) 509–517. [PubMed: 18982643]
40. Taghirad H, Parallel Robots: Mechanics and Control (CRC Press, Boca Raton, 2013).
41. Nguyen CC, Zhou ZL, Antrazi SS and Campbell CE, Efficient computation of forward kinematics and jacobian matrix of a Stewart platform-based manipulator, in IEEE Proc. SOUTH-EASTCON ’91, Vol. 2 (IEEE, 1991), pp. 869–874.
42. Whitney DE, Resolved motion rate control of manipulators and human prostheses, IEEE Trans. Man-Mach. Syst 10(2) (1969) 47–53.
43. Musa MJ, Sharma K, Cleary K and Chen Y, Respiratory compensated robot for liver cancer treatment: Design, fabrication, and benchtop characterization, IEEE/ASME Trans. Mechatronics 27 (2021) 268–279.
44. Bussels B, Goethals L, Feron M, Bielen D, Dymarkowski S, Suetens P and Haustermans K, Respiration-induced movement of the upper abdominal organs: A pitfall for the three-dimensional conformal radiation treatment of pancreatic cancer, Radiother. Oncol 68(1) (2003) 69–74. [PubMed: 12885454]
45. Suramo I, Päivänsalo M and Myllylä V, Cranio-caudal movements of the liver, pancreas and kidneys in respiration, Acta Radiol. Diagn 25(2) (1984) 129–131.
46. Geraghty EM, Boone JM, Mcgahan JP and Jain K, Normal organ volume assessment from abdominal CT, Abdom. Imag 29(4) (2004) 482–490.
47. Slotine JE and Li W, Applied Nonlinear Control (Prentice-Hall, Englewood Cliffs, NJ, 1991).
48. Wang Y, Su H, Harrington K and Fischer G, Sliding mode control of piezoelectric valve regulated pneumatic actuator for MRI-compatible robotic intervention, in ASME 2010 Dynamic Systems and Control Conf. (ASME, 2010), pp. 23–28.
49. Chen Y, Kwok K-W and Tse ZTH, An MR-conditional high-torque pneumatic stepper motor for MRI-guided and robot-assisted intervention, Ann. Biomed. Eng 42(9) (2014) 1823–1833. [PubMed: 24957635]

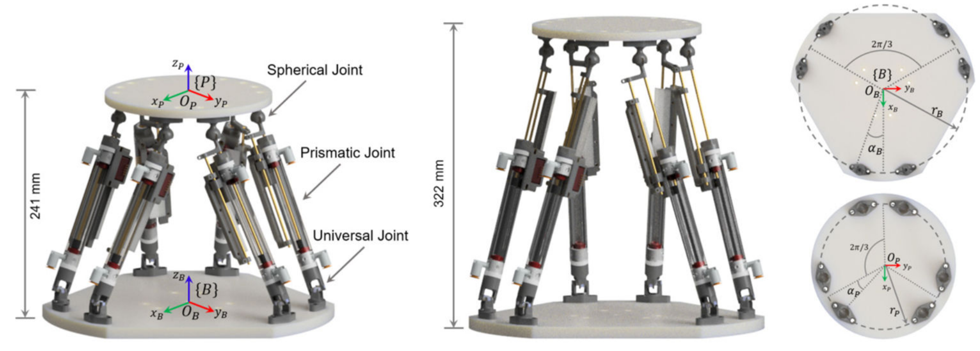

(a) (b) (c)

Fig. 1.

CAD rendering of the MR-conditional parallel robotic platform in the 6-*UPS* Stewart–Gough platform configuration: (a) robot in the homed configuration; coordinate frames are assigned to the center of the fixed base and moving platform at the points O_B and O_P, respectively, (b) robot in the fully extended configuration, (c) (*top*) fixed base geometry, (*bottom*) moving platform geometry.

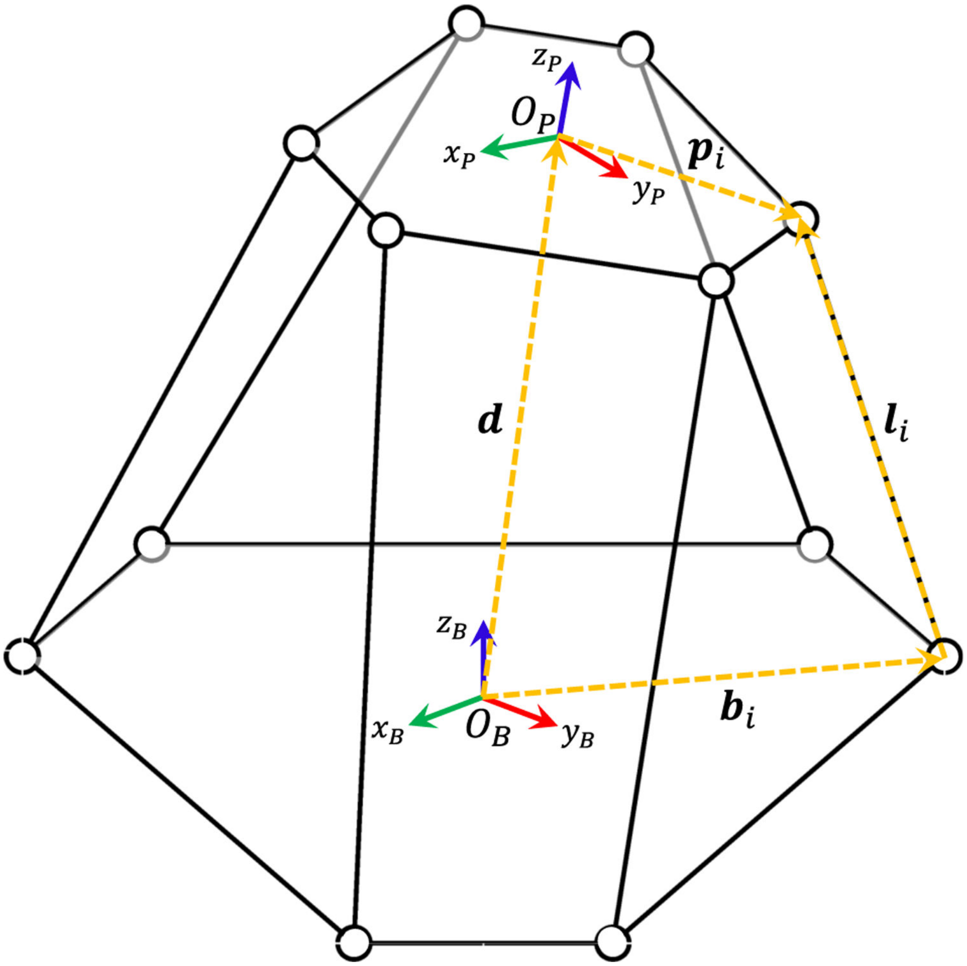

Fig. 2.

Vector diagram for the *i*th limb used to solving the inverse kinematics problem.

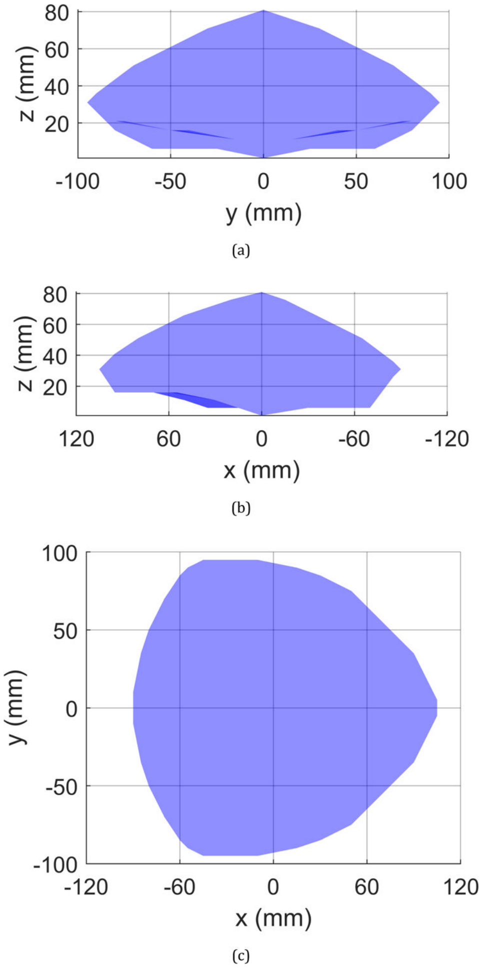

Fig. 3.

Workspace of the parallel robot using the constant orientation representation: (a) view of the workspace in from $Z - Y$ plane, (b) view of the workspace from the $Z - X$ plane, (c) view of the workspace from the $X - Y$ plane.

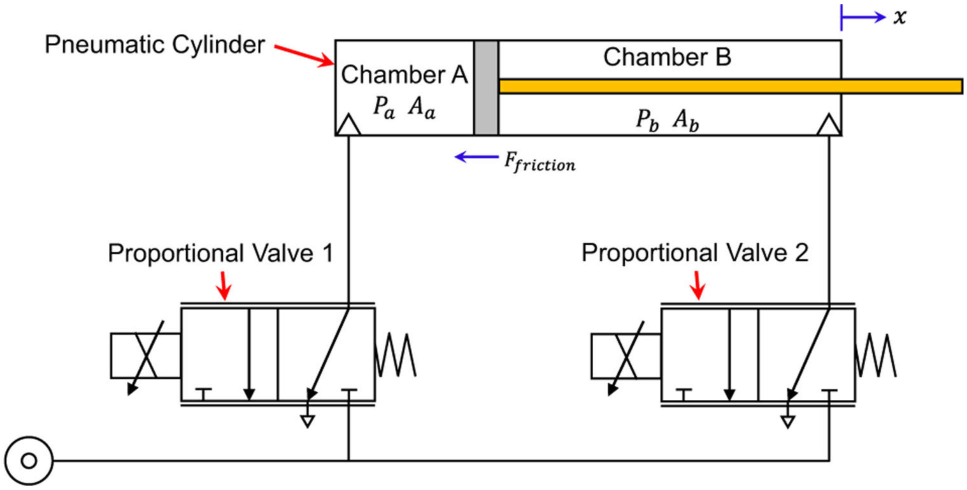

Fig. 4.

Pneumatic circuit diagram of the double-acting cylinder.

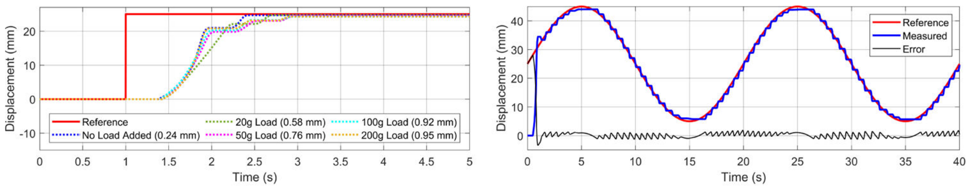

(a) (b)

Fig. 5.

(a) Comparison of set point tracking of the pneumatic cylinder under various loading conditions (steady-state error is given in brackets). (b) Results of the dynamic tracking experiment of the pneumatic cylinder in response to a sinusoidal input.

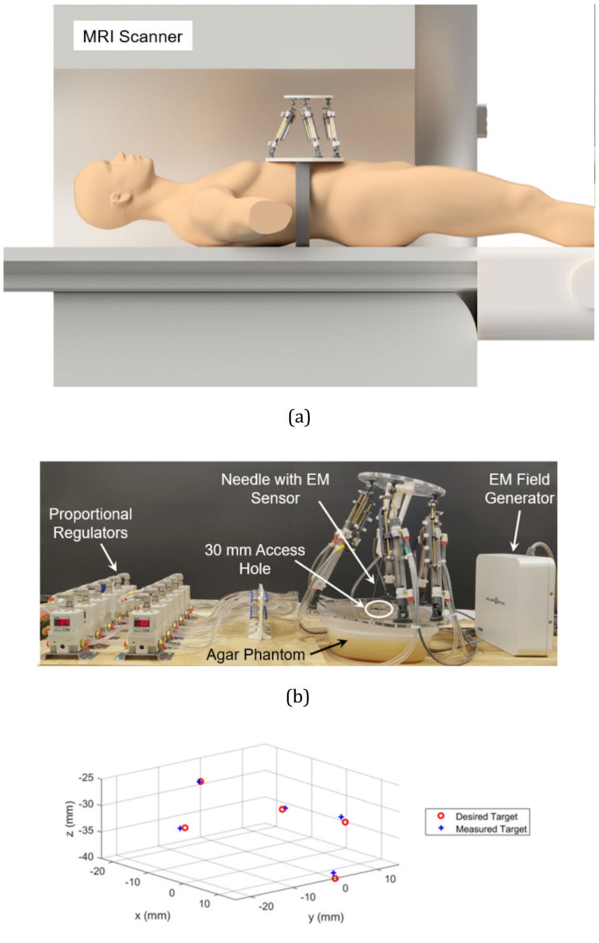

(a)

(b)

(c)

Fig. 6.

(a) CAD rendering of the proposed robot mounted to the patient in the MRI for abdomen interventions. (b) Experimental setup of the tissue-mimic phantom targeting experiment. (c) Phantom targeting experiment result. The red markers indicate the location of the desired target and the blue markers indicate the measured position of the needle tip.

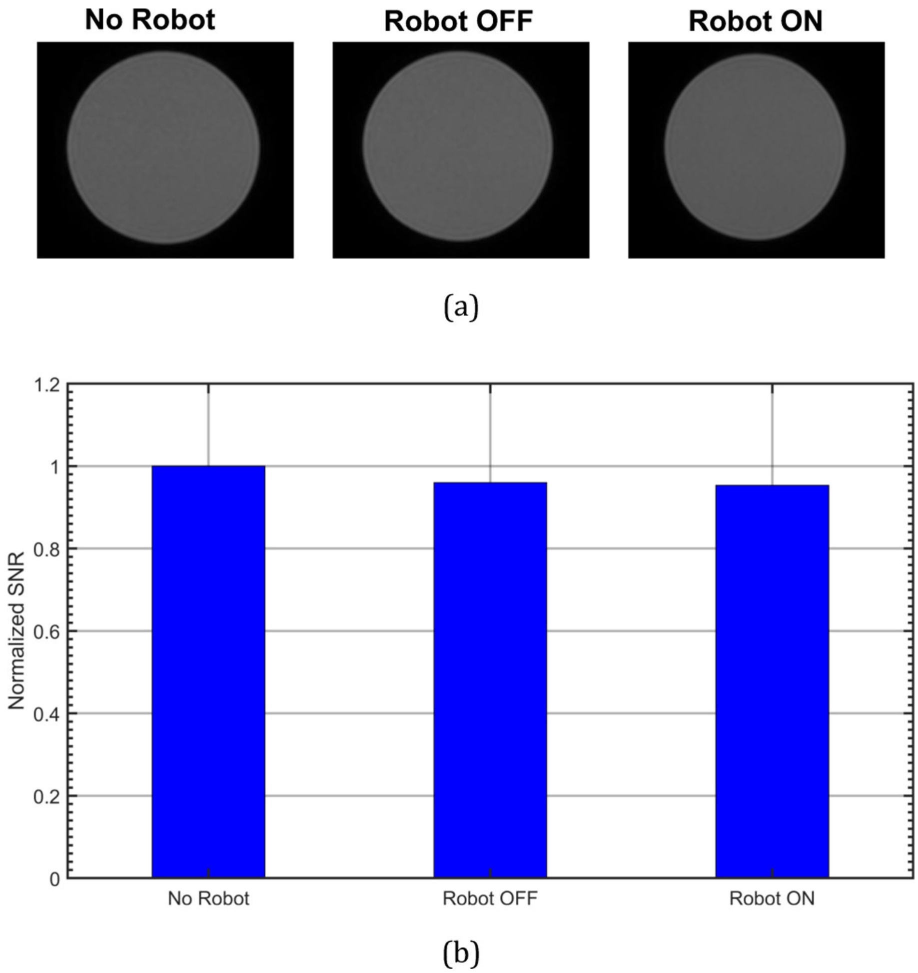

Fig. 7.
(a) 3D gradient echo sequence images of a phantom bottle taken in a 3T Philips MRI scanner; (b) normalized SNR of the MR images. The maximum observed SNR variation was 4.7%.

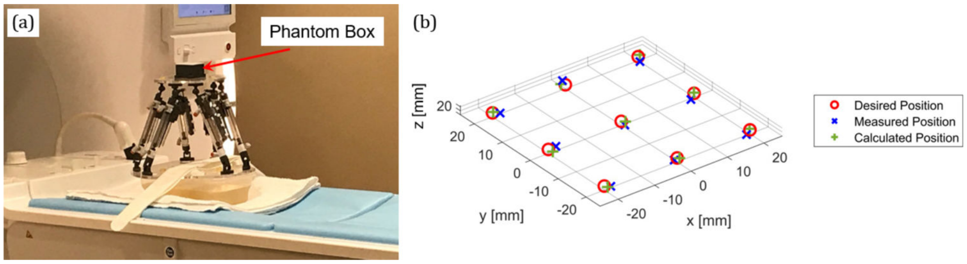

Fig. 8.

(a) Experimental setup of the robot placed in a 3T Philips MRI scanner with a phantom box placed on the moving platform. The phantom box is filled with ultrasound coupling gel; (b) top view of the phantom motion experiment; the red markers indicate the desired phantom position, the blue markers indicate the measured position of the phantom, and the green markers indicate the position of the moving platform calculated offline using the forward kinematics and the recorded encoder data.

Table 1.

Workspace volume comparison.

	Volume (cm^3)	Percent covered by robot
Robot	1016	—
Liver	1710	60%
Spleen	238.4	100%
Kidneys	193.1	100%
Pancreas	87.4	100%

Table 2.

End-effector rotation results.

No.	θ_x	θ_y	θ_z	$\|\text{Error(deg)}\|$
1	5	0	0	1.50
2	−5	0	0	1.62
3	0	5	0	1.79
4	0	−5	0	1.87
5	0	0	5	0.91
6	0	0	−5	1.38
Mean				1.51
Standard deviation				0.32